Hardware-in-the-Loop Simulation System for Space Manipulator Docking: Model, Stability and Experimental Evaluation

Simiao Yu, Shutao Zheng, Yu Yang✉, Zhiyong Qu and Junwei Han
(School of Mechatronics Engineering, Harbin Institute of Technology, Harbin 150001, China)

Abstract: A manipulator-type docking hardware-in-the-loop (HIL) simulation system is proposed in this paper, with further development of the space docking technology and corresponding requirements of the engineering project. First, the structure of the manipulator-type HIL simulation system is explained. The mass and the flexibility of the manipulator has an important influence on the stability of the HIL system, which is the premise of accurately simulating actual space docking. Thus, the docking HIL simulation models of rigid, flexible and flexible-light space manipulators are established. The characteristics of the three HIL systems are studied from three important aspects: the system parameter configuration relation, the system stability condition and the dynamics frequency simulation ability. The key conclusions obtained were that the system satisfies stability or reproduction accuracy. Meanwhile, the influence of different manipulators on the system stability is further analyzed. The accuracy of the calculated results is verified experimentally.

Key words: manipulator docking; hardware-in-the-loop (HIL) simulation; parameter configuration; stability condition; dynamics frequency simulation capability
CLC number: TP 29 **Document code**: A **Article ID**: 1004-0579(2020)01-0089-14

The docking between the space station and spacecraft is one of the key technologies for material transportation, space station construction and system maintenance. Because of the complex structure and task of the space station, the space manipulator is the main means of realizing space docking and other on-orbit servicing for its dexterity and broad capabilities[1-3].

The terminal of the space manipulator is equipped with an end-effector. The capture, drag and other docking operations on the target-adapter equipped on the spacecraft are achieved by using the end-effector[4-5]. It is necessary to simulate the space manipulator docking on the ground to ensure the success of real docking. HIL simulation is often used to simulate the docking process for it integrates the flexibility of numerical simulation and the fidelity of physical simulation. The stability of the hardware-in-the-loop (HIL) simulation system is not only one of the most critical characteristics, but also the premise of simulating the actual space docking accurately.

HIL simulations are the world's leading-edge technology[6-10], and there are relatively few reported references. Refs. [11-12] simulated the docking process of two rigid mechanisms using a serial robot, and used gravity compensation method to simulate the microgravity environment. Then, they validated the effectiveness of the simulation system experimentally[11-12]; there were no analyses of system characteristics in the refer-

Received 2018-09-20
Supported by the National Natural Science Foundation of China(51475116)
✉ Author for correspondence, lecturer, Ph. D.
E-mail: yangyu1980hit@163.com
DOI: 10.15918/j.jbit1004-0579.18134

ences. Ref. [13] proposed a Taylor series compensation method based on a low order model for the system instability, which is caused by the response delay of the robot. Ref. [14] proposed the damping and elastic contact force compensation method for the system instability problems. Refs. [13, 14] only improved and analyzed the influence of system lag on stability; the authors didn't research the influence of parameters on stability and systematic stability conditions. Ref. [15] established the serial robot model as a second-order delay system, and the critical delay and associated frequency were derived as a function of the satellites' mass, the contact stiffness and damping parameters. Then, the value relation of indices which satisfied the stability was obtained by using pole location method in Refs. [15]. Refs. [16 – 19] established the HIL simulation system model based on the docking between two rigid spacecrafts. The stability conditions and the frequency range of the dynamics, which can be simulated in the system, were obtained.

In the above references, the docking objects are two rigid spacecraft. In this study, there are more objects and the flexibility of the manipulator is considered. In addition, while the references use the series robot as drive systems, this study uses the parallel robot to simulate the process of the space manipulator docking for its quick response speed. When the manipulator is rigid, the docking model is similar to the rigid docking model in the references. However, the manipulator is usually flexible, and the flexibility and mass of the manipulator have a great influence on the docking dynamics model and the HIL model. The model and stability analyses of the HIL simulation system becomes more complex because of the difference between the simulated objects and the drive system. In view of the new application background, this study considers the flexibility and mass characteristics of the manipulator. Furthermore, the HIL simulation system models of rigid, flexible and flexible-light forms of the manipulator are proposed and established. Then, the HIL system stability and the influences of different manipulator forms on the system stability are obtained and compared from both simulation and experimental aspects.

1 Structure and Principle of Hardware-in-the-Loop Simulation System for Space Manipulator Docking

The space docking system consists of a spacecraft, a manipulator, an end-effector and a space station, as shown in Fig. 1. The docking success depends on the relative position of the end-effector and the target-adapter (equipped on the spacecraft). The structure of the HIL simulation system is proposed, as shown in Fig. 2. The physical objects consist of an end-effector, a target-adapter, a 6-DOF parallel robot, a force sensor and a frame.

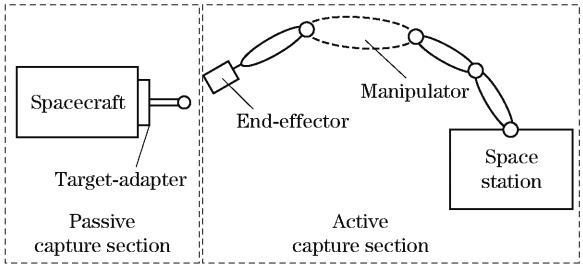

Fig. 1 Space docking system

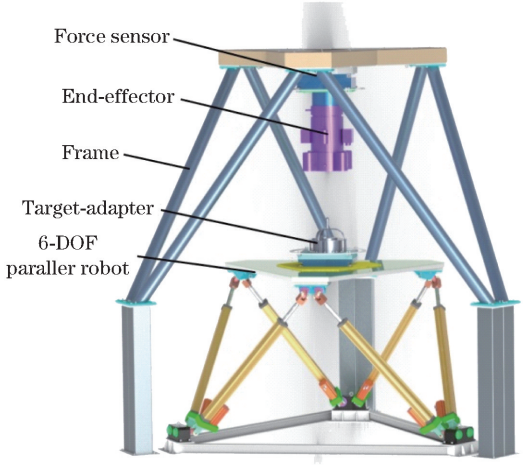

Fig. 2 Structure of the HIL simulation system

The system simulation principle is as follows:

the collision force of the docking mechanism is measured by the force sensor. The sensor is fixed on the frame, which ensures that the sensor only measures the collision force after removing the gravity value of the end-effector. The kinematic characteristics of the space station, the manipulator, the end-effector and the spacecraft are calculated by the dynamics. Then the relative motion parameters of the target-adapter and the end-effector are calculated by the dynamics and reproduced by the parallel robot.

2 Modeling of the Hardware-in-the-Loop Simulation System

The joints of the manipulator are locked when the space manipulator is docking, which reduces the adverse effect of residual vibration at the terminal of the manipulator. Therefore, the movement of the manipulator in the docking process is mainly represented by elastic deformation. Based on this consideration, the manipulator can be equivalent to the mass-spring-damping system. According to the attitude of the manipulator, the equivalent mass, stiffness and damping parameters of the manipulator can be obtained by the lumped parameter method. The contact stiffness, the manipulator stiffness and the dynamics of the six degrees of freedom are decoupled. Therefore, take the single degree of freedom as an example to analyze the characteristics of the system.

2.1 Docking dynamics modeling

2.1.1 Rigid manipulator form system

The principle of the single degree of freedom docking is shown in Fig. 3. The mechanisms in Fig. 3 are on a horizontal line, which just intuitively represents the docking principle in this direction, but does not indicate the actual relative position of the mechanisms. When the manipulator is rigid, the space station, the manipulator and the end-effector can be regarded as a whole. The positive direction of the system is defined as the positive direction of x_1.

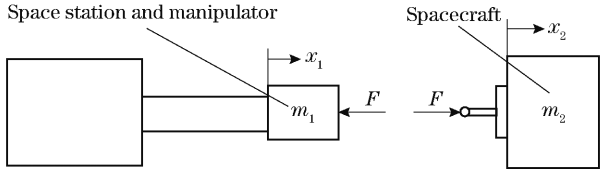

Fig. 3 Principle schematic diagram of the rigid docking

The relative displacement of the spacecraft and the end-effector is

$$x = x_2 - x_1 = \iint \left(\frac{F}{m_2} + \frac{F}{m_1}\right)\mathrm{d}t = \iint \left(\frac{F}{m}\right)\mathrm{d}t \quad (1)$$

where $m = \dfrac{m_1 m_2}{m_1 + m_2}$.

After the Laplace transform, the docking dynamics equation is

$$\frac{X}{F} = \frac{1}{ms^2} \quad (2)$$

where x_1 and x_2 are the displacements of the spacecraft and the end-effector, respectively. F is the force measured by force sensor, m_1 is the comprehensive mass of the end-effector, the manipulator and the space station, and m_2 is the mass of the spacecraft.

2.1.2 Flexible manipulator form system

The principle of the single degree of freedom docking is shown in Fig. 4.

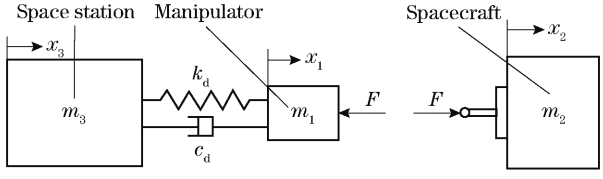

Fig. 4 Principle schematic diagram of the flexible docking

The dynamics equation of the manipulator is

$$m_1\ddot{x}_1 + c_d(\dot{x}_1 - \dot{x}_3) + k_d(x_1 - x_3) = F \quad (3)$$

where x_1 and x_3 are the displacements of the end-effector and the space station, respectively; m_1 is the comprehensive mass of the end-effector and the manipulator; c_d and k_d are the damping and stiffness of the manipulator in one direction, respectively.

Laplace transformation of Eq. (3)

$$m_1 s^2 X_1 + c_d s(X_1 - X_3) + k_d(X_1 - X_3) = F \quad (4)$$

The dynamics equation of the space station is

$$m_3\ddot{x}_3 - c_d(\dot{x}_1 - \dot{x}_3) - k_d(x_1 - x_3) = 0 \quad (5)$$

Laplace transformation of Eq. (5)

$$m_3 s^2 X_3 - c_d s(X_1 - X_3) - k_d(X_1 - X_3) = 0 \quad (6)$$

Using Eq. (4) and Eq. (6), the following relationship is given as

$$\frac{X_1}{F} = \frac{m_1 s^2 + c_d s + k_d}{s^2[m_1 m_3 s^2 + (m_1 + m_3)c_d s + (m_1 + m_3)k_d]} \quad (7)$$

The dynamics equation of the spacecraft is

$$m_2\ddot{x}_2 = -F \quad (8)$$

where x_2 is the displacement of spacecraft; m_2 and m_3 are the masses of the spacecraft and space station, respectively.

The Laplace transform of Eq. (8) is

$$m_2 s^2 X_2 = -F \quad (9)$$

The relative displacement between the spacecraft and the end-effector is

$$x = x_2 - x_1 \quad (10)$$

Using Eq. (7), Eq. (9) and Eq. (10), the docking dynamics equation can be written as

$$\frac{X}{F} = -\frac{\frac{m_3^*}{k_d}s^2 + \frac{c_d}{k_d}s + 1}{m_2^* s^2\left(\frac{m_1^*}{k_d}s^2 + \frac{c_d}{k_d}s + 1\right)} \quad (11)$$

where $m_1^* = \frac{m_1 m_3}{m_1 + m_3}$, $m_2^* = \frac{m_1 m_2 + m_2 m_3}{m_1 + m_2 + m_3}$, $m_3^* = \frac{m_1 m_3 + m_2 m_3}{m_1 + m_2 + m_3}$.

2.1.3 Flexible-light manipulator form system

In general, compared to the mass of the space station, the masses of the manipulator and the end-effector are very small. At this point, the dynamics characteristics are almost unchanged when neglecting the masses of the manipulator and the end-effector. However, the characteristics of the HIL simulation system will be affected by neglecting the masses. Thus, the corresponding system characteristics are studied, with the dynamics equation written as

$$\frac{X}{F} = -\frac{\frac{m_2^*}{k_d}s^2 + \frac{c_d}{k_d}s + 1}{m_2^* s^2\left(\frac{c_d}{k_d}s + 1\right)} \quad (12)$$

where $m_1 = 0$, $m_1^* = 0$, $m_2^* = m_3^* = \frac{m_2 m_3}{m_2 + m_3}$.

2.2 Equivalent model of 6-DOF parallel robot

The dynamics and position control models of the 6-DOF parallel robot are shown in Fig. 5[20-21]. The frequency characteristics of the 6-DOF parallel robot are the same as the nominal system at each degree of freedom[18]. The nominal system function can be written as

$$G(s) = \frac{K_v}{\left(\frac{s}{K_v} + 1\right)\left(\frac{s^2}{\omega_n^2} + \frac{2\xi}{\omega_n}s + 1\right)} \quad (13)$$

where K_v is the open-loop speed gain of the system, ω_n and ξ are the natural frequency and damping ratio of the system, respectively.

The equivalent model of 6-DOF parallel robot is shown in Fig. 6.

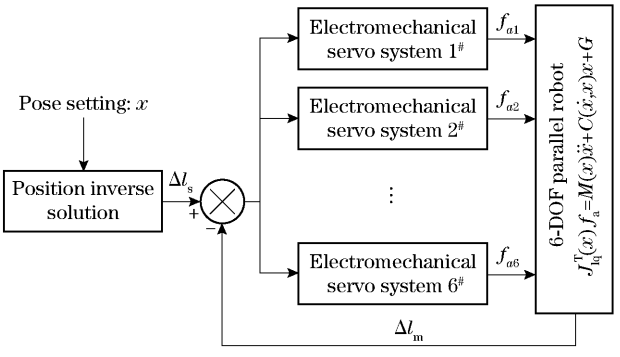

Fig. 5 Dynamics and position control principle schematic diagram of the 6-DOF parallel robot

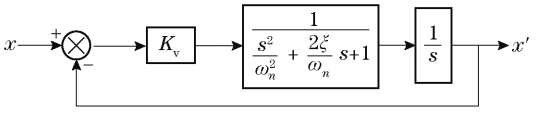

Fig. 6 Equivalent model of the 6-DOF parallel robot

2.3 Collision force model

The collision force F obtained by the sensor is expressed as

$$F = c\dot{x}' + kx' \quad (14)$$

where k and c are the contact stiffness and the damping of docking mechanism, respectively; x'

and $\dot{x}'$ are the displacement and velocity of 6-DOF parallel robot, respectively.

3 Stability Analysis of Hardware-in-the-Loop Simulation System

3.1 Stability analysis of rigid manipulator system

Rigid manipulator HIL system (referred to as the R system) model can be established based on the docking dynamics model, the 6-DOF parallel robot control model and the collision force model. The model of the single degree of freedom system is shown in Fig. 7.

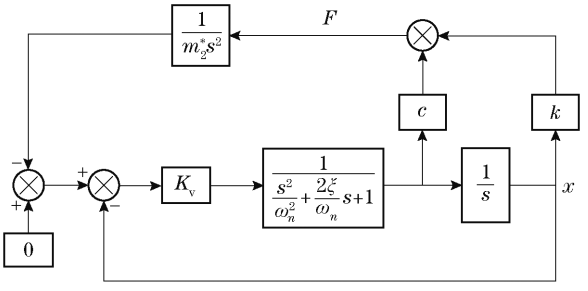

Fig. 7 Single degree of freedom R system diagram

The open-loop transfer function of the system is

$$G_k(s)=\frac{(K_v cs+K_v k)}{ms^2\left[s\left(\frac{s^2}{\omega_n^2}+\frac{2\xi}{\omega_n}s+1\right)+K_v\right]} \tag{15}$$

The stability condition of the system can be obtained by the Routh-criteria

$$\begin{cases} 0<K_v<2\xi\omega_n \\ k<K_v c \\ m>\dfrac{2\xi}{\omega_n}\cdot\dfrac{2\xi\omega_n c-k}{2\xi\omega_n-K_v} \\ m>\dfrac{K_v(2\xi\omega_n c-k)^2}{(K_v c-k)(2\xi\omega_n-K_v)} \end{cases} \tag{16}$$

In the second line of Eq. (16), the relation among the contact stiffness and damping of the docking mechanism and the open-loop gain of the robot are obtained, which satisfies the stability condition. It is explained that the appropriate parameters of physical objects are the prerequisite for the simulation of the rigid manipulator system.

3.2 Stability analysis of flexibility manipulator system

Flexibility manipulator HIL system, also referred to as the F system. The model of the single degree of freedom system is shown in Fig. 8.

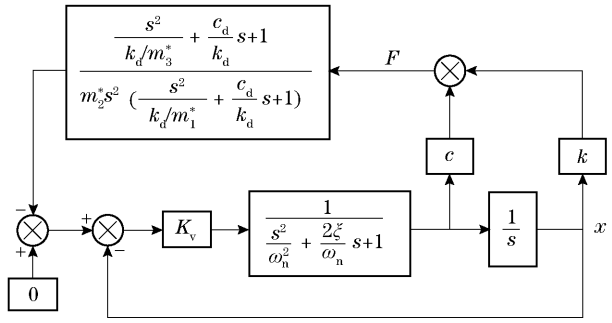

Fig. 8 Single degree of freedom F system diagram

The open-loop transfer function of the system is

$$G_k(s)=\frac{(K_v cs+K_v k)\left(\frac{m_3^*}{k_d}s^2+\frac{c_d}{k_d}s+1\right)}{m_2^* s^2\left[s\left(\frac{s^2}{\omega_n^2}+\frac{2\xi}{\omega_n}s+1\right)+K_v\right]\left(\frac{m_1^*}{k_d}s^2+\frac{c_d}{k_d}s+1\right)} \tag{17}$$

The open-loop transfer function adds a second order differentiation element and the second order oscillating element after considering the flexibility and mass characteristics of the manipulator. The parameters of the two elements are determined by the mass and stiffness of the manipulator. The parameter configuration relation is analyzed to satisfy the better stability of the system.

3.2.1 Parameter configuration analysis of system with better characteristics

The open-loop transfer function of the system can be obtained by modifying the transfer function of the 6-DOF parallel robot

$$G_k(s)=\frac{k}{m_2^*}\times\frac{\left(\frac{s}{k/c}+1\right)\left(\frac{m_3^*}{k_d}s^2+\frac{c_d}{k_d}s+1\right)}{s^2\left(\frac{s}{K_v}+1\right)\left(\frac{m_1^*}{k_d}s^2+\frac{c_d}{k_d}s+1\right)\left(\frac{s^2}{\omega_n^2}+\frac{2\xi-K_v/\omega_n}{\omega_n}s+1\right)} \tag{18}$$

Make $\frac{1}{T_1}=\omega_n$, $\frac{1}{T_2}=\frac{k}{c}$, $\frac{1}{T_3}=K_v$, $\frac{1}{T_4}=\sqrt{\frac{k_d}{m_3^*}}$, $\frac{1}{T_5}=\sqrt{\frac{k_d}{m_1^*}}$. In addition, in Eq. (11) $m_3^*>m_1^*$, therefore, $\frac{1}{T_4}<\frac{1}{T_5}$.

According to the actual objects, the parameters usually have the following relations: $m_3>m_2>m_1>200$ kg. Using frequency to represent K_v and ω_n, K_v is approximately 10 Hz, and ω_n is greater than 60 Hz. The stiffness of the flexible manipulator k_d is generally no higher than 10^6 N/m magnitude (higher than this magnitude can be considered as rigid manipulator). According to the relation of parameters, the corner frequencies of partial elements have the following relation

$$\frac{1}{T_4}<\frac{1}{T_5}<\frac{1}{T_3}<\frac{1}{T_1} \tag{19}$$

When the slope around gain cross-over frequency is -20 dB/dec, a larger stability margin and high reproduction accuracy can be obtained. The open-loop Bode diagram of the system, representing $1/T_2$ and other corner frequencies, is shown in Fig. 9.

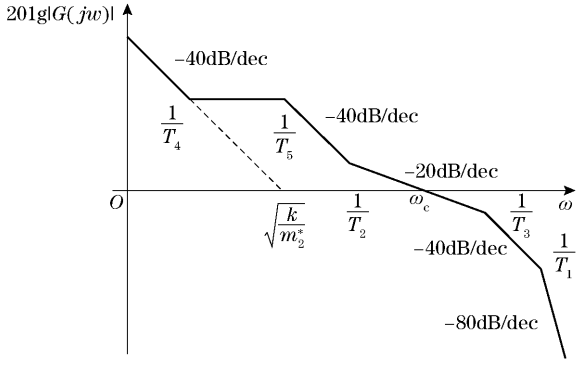

Fig. 9 Bode diagram of the system under condition of Eq. (20)

The parameter configuration relations are

$$\begin{cases}\dfrac{1}{T_4}<\dfrac{1}{T_5}<\dfrac{1}{T_2}<\dfrac{1}{T_3}<\dfrac{1}{T_1}\\ \log_{10}\left(\left|G\left(\dfrac{1}{T_2}\right)\right|\right)>0\\ \log_{10}\left(\left|G\left(\dfrac{1}{T_3}\right)\right|\right)<0\end{cases} \tag{20}$$

3.2.2 System stability condition

Under some conditions, the parameters can't satisfy the above conclusions. The stability condition of the system is further studied. The system model becomes complex and the stability conditions are difficult to obtain after considering the flexibility of the manipulator.

In order to maintain an effective simulation, the physical parameter of k in the actual system should be relatively small, which ensures the cross-over frequency in low-frequency or mid-frequency region. The natural frequency of the 6-DOF parallel robot ω_n is much larger than the corner frequencies of other elements and ω_c. Thus, the second order oscillatory element of the robot model can be ignored. The denominator of the closed-loop transfer function of the system is

$$\begin{aligned}D(s)=&\frac{m_1^*m_2^*}{K_v}s^5+\left(\frac{m_2^*c_d}{K_v}+m_1^*m_2^*\right)s^4+\\&\left(\frac{k_dm_2^*}{K_v}+m_2^*c_d+m_3^*c\right)s^3+(k_dm_2^*+cc_d+\\&m_3^*k)s^2+(ck_d+c_dk)s+kk_d\end{aligned} \tag{21}$$

where $c_d/K_v\ll m_1^*$

The stability condition of the system can be obtained by the Routh-criterion as shown in

$$\begin{cases}0<K_v<2\xi\omega_n\\ K_v>\max\left(\dfrac{cc_d/m_3^*+k}{m_2^*c_d/m_3^*+c},\ \dfrac{k}{c_dk/k_d+c}\right)\\ m_1^*<\dfrac{(k_dm_2^*+cc_d+m_3^*k)\left(c_dm_2^*+cm_3^*-\dfrac{cc_d+m_3^*k}{K_v}\right)}{m_2^*(ck_d+c_dk-kk_d/K_v)}\\ (k_dm_2^*+cc_d+m_3^*k)>\dfrac{(ck_d+c_dk-kk_d/K_v)}{\left(c_dm_2^*+cm_3^*-\dfrac{cc_d+m_3^*k}{K_v}\right)}\times\\ \qquad m_1^*m_2^*+\dfrac{\left(c_dm_2^*+cm_3^*-\dfrac{cc_d+m_3^*k}{K_v}\right)}{(ck_d+c_dk-kk_d/K_v)}kk_d\end{cases} \tag{22}$$

If the R system is stable, then K_v is required to be greater than k/c. This is because the initial phase angle of the R system is $-180°$, if K_v is less than k/c, the phase at the point of over-cross frequency less than $-180°$, then the system is unstable. Based on Eq. (22), the system can still be

stable under the condition of $k/(c + c_d k/k_d) < K_v < k/c$, this is because when c_d is large, the second order differentiation element and the second order oscillation element, which are determined by the parameters of the manipulator, can add the positive phase angle in low-frequency and mid-frequency regions. The positive phase angle can also compensate for the negative phase angle that is produced by the inertial element at the point of the cross-over frequency. The stability of the system is improved and the restrictions on the physical parameters are relaxed after considering the flexibility characteristics of the manipulator.

3.3 Stability analysis of flexibility-light manipulator system

The flexibility-light manipulator HIL system is also referred to as the F-L system. The single degree of freedom system is shown in Fig. 10. The open-loop transfer function of the system is expressed as

$$G_k(s) = \frac{k}{m_2^*} \times \frac{\left(\frac{s}{k/c}+1\right)\left(\frac{m_2^*}{k_d}s^2+\frac{c_d}{k_d}s+1\right)}{s^2\left(\frac{s}{K_v}+1\right)\left(\frac{c_d}{k_d}s+1\right)\left(\frac{s^2}{\omega_n^2}+\frac{2\xi-K_v/\omega_n}{\omega_n}s+1\right)} \tag{23}$$

According to Eq. (23), the second order oscillation element changes into a first order inertial element after ignoring the mass.

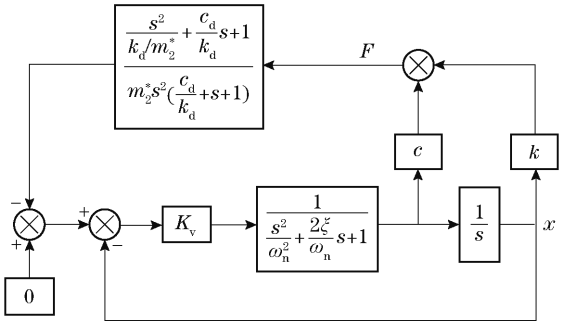

Fig. 10 Single degree of freedom F-L system diagram

3.3.1 Parameter configuration analysis of system with better characteristics

Let $\frac{1}{T_1}=\omega_n, \frac{1}{T_2}=\frac{k}{c}, \frac{1}{T_3}=K_v, \frac{1}{T_4}=\sqrt{\frac{k_d}{m_3^*}}, \frac{1}{T_5}=\frac{k_d}{c_d}$. Based on the parameter relations, the corner frequencies of the partial elements have the following relation as

$$\frac{1}{T_4}<\frac{1}{T_3}<\frac{1}{T_1} \tag{24}$$

In order to ensure the slope around gain cross-over frequency is -20 dB/dec. The open-loop Bode diagrams of the system are shown in Fig. 11 and Fig. 12, which consist of $1/T_2$, $1/T_5$ and other corner frequencies. The parameter configuration relations in Fig. 11 are as follows.

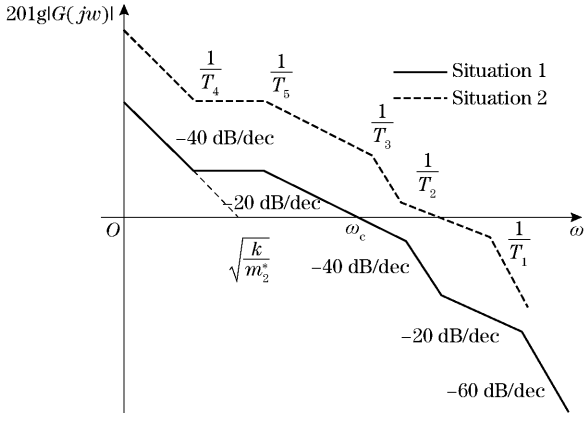

Fig. 11 Bode diagram of the system under condition of Eq. (25)

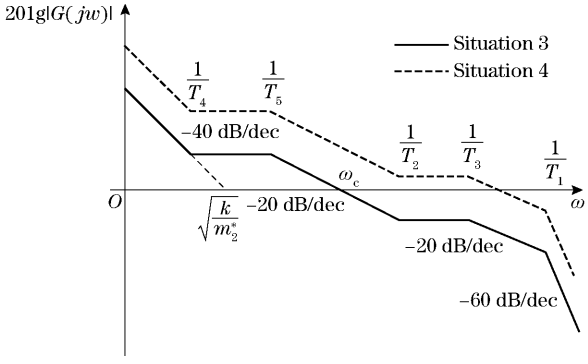

Fig. 12 Bode diagram of the system under condition of Eq. (26)

$$\begin{cases} \frac{1}{T_4}<\frac{1}{T_5}<\frac{1}{T_3}<\frac{1}{T_2}<\frac{1}{T_1} \\ \text{Situation 1}: \log_{10}\left(\left|G\left(\frac{1}{T_5}\right)\right|\right)>0 \\ \quad \log_{10}\left(\left|G\left(\frac{1}{T_3}\right)\right|\right)<0 \\ \text{Situation 2}: \log_{10}\left(\left|G\left(\frac{1}{T_2}\right)\right|\right)>0 \\ \quad \log_{10}\left(\left|G\left(\frac{1}{T_1}\right)\right|\right)<0 \end{cases} \tag{25}$$

The parameter configuration relations in Fig. 12 are shown as

$$\begin{cases} \dfrac{1}{T_4} < \dfrac{1}{T_5} < \dfrac{1}{T_2} < \dfrac{1}{T_3} < \dfrac{1}{T_1} \\ \text{Situation 3: } \log_{10}\left(\left|G\left(\dfrac{1}{T_5}\right)\right|\right) > 0 \\ \qquad \log_{10}\left(\left|G\left(\dfrac{1}{T_2}\right)\right|\right) < 0 \\ \text{Situation 4: } \log_{10}\left(\left|G\left(\dfrac{1}{T_3}\right)\right|\right) > 0 \\ \qquad \log_{10}\left(\left|G\left(\dfrac{1}{T_1}\right)\right|\right) < 0 \end{cases} \tag{26}$$

Curves 2 and 4 of situations 2 and 4, respectively, are the shift results of curves 1 and 3 of situations 1 and 3, respectively. The second order oscillation element of the open-loop transfer function is converted to a first order inertial element and the slope changes from -40 dB/dec to -20 dB/dec of this element, which makes the situation of slope around gain cross-over frequency of -20 dB/dec become more frequent. The requirements for the parameters are relaxed when the system has the better characteristics.

3.3.2 System stability condition

ω_n is much larger than the corner frequencies of other elements and the cross-over frequency ω_c in the low-frequency or mid-frequency region. The stability condition of the system can be obtained through the Routh-criterion after simplification. While $K_v > \dfrac{k}{c + \left(\dfrac{k}{k_d}\right)^2 c_d}$, the stability condition is

$$\begin{cases} 0 < K_v < 2\xi\omega_n \\ K_v > \dfrac{k}{c_d\left(\dfrac{k}{k_d}\right)^2 + c} \\ m_2^* > \dfrac{(c_d^2 k - K_v c c_d (c + c_d))}{(k_d + K_v(c + c_d))(k + k_d)} \\ m_2^* > \dfrac{(c_d k + c k_d)(c_d^2 k - K_v c c_d (c + c_d))}{(k_d/K_v + c + c_d)(K_v(c k_d^2 + c_d k^2) - k k_d^2)} \end{cases} \tag{27}$$

While $K_v < \dfrac{k}{c + \left(\dfrac{k}{k_d}\right)^2 c_d}$, the stability condition is

$$\begin{cases} 0 < K_v < 2\xi\omega_n \\ \dfrac{k}{c + c^2/c_d} < K_v < \dfrac{k}{c_d\left(\dfrac{k}{k_d}\right)^2 + c} \\ 0 < m_2^* < \dfrac{(c_d k + c k_d)(c_d^2 k - K_v c c_d (c + c_d))}{(k_d/K_v + c + c_d)(K_v(c k_d^2 + c_d k^2) - k k_d^2)} \\ \dfrac{k}{c} > \dfrac{k_d}{c_d} \end{cases} \tag{28}$$

3.4 Analysis of dynamics frequency range based on stability and reproduction accuracy

From the parameter configuration analyses and stability conditions can be known, a system with a large stiffness or a small mass will make the system unstable.

The values of stiffness and mass limit the range of dynamics frequency ω_0. Meanwhile, the dynamics frequency is also limited by the bandwidth frequency ω_b of the parallel robot. When the dynamics frequency is large, the system attenuation is large and the reproduction accuracy is low. The parameters can be further configured by obtaining the dynamics frequency range that satisfies the stability and reproduction accuracy. Then, the differences among the different systems are further evaluated. In the HIL system, the dynamics frequency range (indicates the reproduction ability of meeting the stability and accuracy) simulated by a parallel robot can be obtained by the analysis.

Based on the ranges of the simulated parameters, the mass of the space station ranges from 10^3 kg to 10^4 kg and the step length is 1 000 kg. The mass of the spacecraft ranges from 10^3 kg to 10^4 kg and the step length is 1 000 kg. The mass of the manipulator ranges from 100 kg to 500 kg and the step length is 100 kg. In each mass group, the contact stiffness ranges from 5 000 N/m to 2×10^5 N/m and the step length is 5 000 N/m. The

manipulator's stiffness ranges from 7 000 N/m to 2.8×10^5 N/m and the step length is 7 000 N/m. The contact damping and manipulator damping parameters are determined by the damping ratio (the damping ratio of the object is approximately 0.05 to 0.2). With a goal of achieving system stability and a reproduction deviation of no more than 15%, the analysis process is shown in Fig. 13.

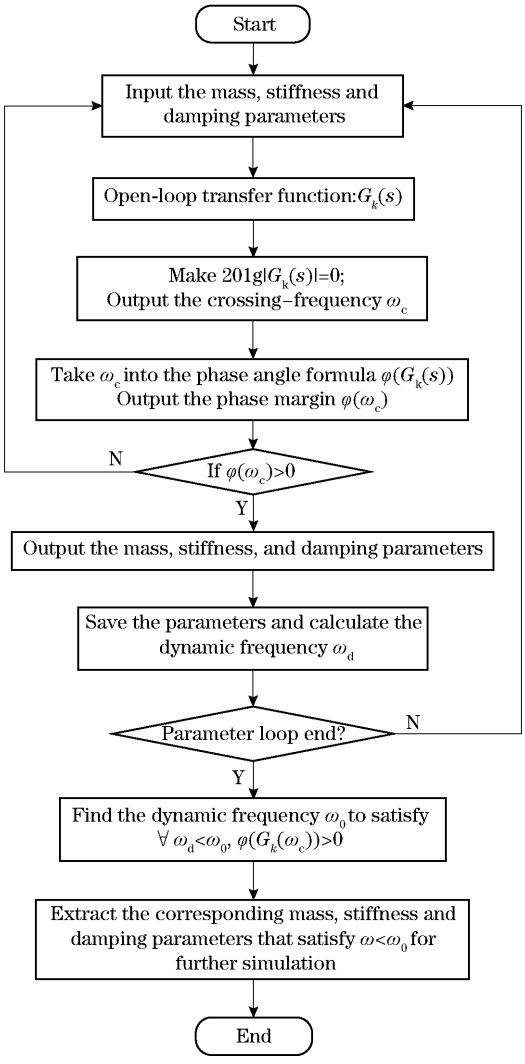

Fig. 13 Dynamics frequency analysis based on the phase margin

From the analysis shown in Fig. 13, the dynamics frequency range which can ensure the stability of the system is obtained. Then, the system reproduction accuracy is simulated and analyzed under the models shown in Fig. 7, Fig. 8 and Fig. 10. The initial offset of the target-adapter relative to the end-effector is set to 10 mm (the initial offset of the platform is 10 mm), and then enters the simulation process. The theoretical relative displacement of the target-adapter from the end-effector (which means the dynamics process without the participation of the parallel robots) and the simulated displacement of the platform can be obtained. Taking the R system as an example, the two curves obtained are shown in Fig. 14.

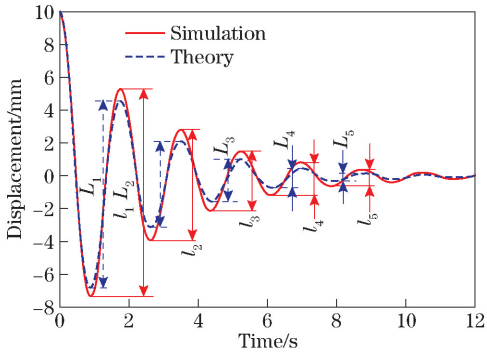

Fig. 14 Oscillating amplitude diagram of the curves

When the dynamics damping ratio is approximately 0.05, the displacement curves tend stabilize after several oscillation periods, so the amplitudes of the first five periods are used to calculate the reproduction deviation. The calculation equation of the reproduction deviation is

$$\eta = \left(\frac{l_1 + l_2 + l_3 + l_4 + l_5}{L_1 + L_2 + L_3 + L_4 + L_5} - 1\right) \times 100\% \,, \tag{29}$$

where l_1, l_2 and l_3 are the amplitude of the theoretical curve and L_1, L_2 and L_3 are the amplitude of the simulation curve.

Parameters sets extracted from Fig. 13 are used for simulation. Target simulation deviation no more than 15%, the calculated docking dynamics frequency range of the three systems is shown in

$$\begin{cases} \text{R system}: \omega_0 \leqslant 0.07\omega_b \\ \text{F system}: \omega_{0high} \leqslant 0.2\omega_b \\ \text{F-L system}: \omega_0 \leqslant 0.25\omega_b \end{cases} \tag{30}$$

Within this frequency range, the number of parameter sets meeting the simulation accuracy accounts for 90% or more of the total number of parameter sets.

The F-L system has better characteristics which can simulate relatively higher contact stiffness and manipulator stiffness. Therefore, the reproduction frequency is higher.

4 Influence of Different Forms of Manipulator on System Stability and the Experimental Verification

Aspects of parameter configuration, system stability condition and the dynamics frequency simulation capability are compared between the different forms of the manipulator. Then, the conclusions are verified by experiments.

4.1 Experimental system

The experiment facilities of the HIL simulation system are shown in Fig. 15. Due to classified reasons, pictures of the end-effector and the target-adapter can't be provided, and pictures of the other main structures are presented separately.

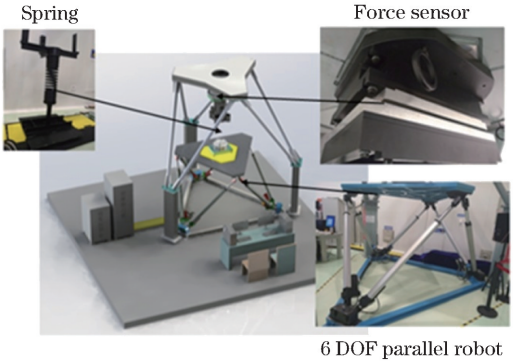

Fig. 15 Experiment facilities of HIL simulation system

In order to study the effects of different physical contact stiffnesses and damping parameters on system characteristics and to obtain the full oscillation period, two springs (of different stiffness) are selected to simulate the collision process of the docking mechanism. The initial displacement offset of the 6-DOF parallel robot is 5 mm or 10 mm in the vertical direction, then enters the dynamics calculation process to obtain the relative motion of the docking mechanism. Then, the oscillation process is reproduced by the robot. In the experiment, the Xpc real-time simulation system in MATLAB (United States) is applied, and the sampling period is set to 1 ms. The upper computer uses LabVIEW (United States) software to edit visual parameter interfaces.

4.2 Comparison analysis and experimental verification

4.2.1 Stability condition verification

In this study, the stability conditions of the system are obtained by simplification. The F system is taken as an example to verify the effectiveness of the proposed method. The experimental parameters are shown in parameter-1 of Tab. 1.

Based on the second line in Eq. (22), c_d should be greater than 422 N/(m/s), which can ensure the system stability. If set c_d as 400 N/(m/s) and 600 N/(m/s), respectively, then $\left(K_v - \frac{cc_d/m_3^* + k}{m_2^* c_d/m_3^* + c}\right)$ is -0.8 and 5, respectively. Other rules satisfy the stability conditions. The displacement curves of the two conditions are shown

Tab. 1 Parameters used in the experiment

Parameter		m_1/kg	m_2/kg	m_3/kg	k_d/(N·m^{-1})	c_d/(N·(m/s)$^{-1}$)	k/(N·m^{-1})	c/(N·(m/s)$^{-1}$)
Parameter-1		200	2 000	8 000	6 000	1 000	70 000	1 000
Parameter-2		400	3 000	10 000	2 000	400/600	70 000	1 000
Parameter-3		400	3 000	10 000	2 000	200	7 000	500
Parameter-4	R system	—	600/1 000	600/1 000	—	—	7 000	500
	F system	100	1 000	4 000	6 000/10 000	300/400	7 000	500
	F-L system	—	100	4 000	30 000/40 000	1 000/1 200	70 000	1 000

in Fig. 16. Based on Fig. 16, when K_v is less than $\frac{cc_d/m_3^* + k}{m_2^* c_d/m_3^* + c}$, the system is unstable. Conversely, the system is stable.

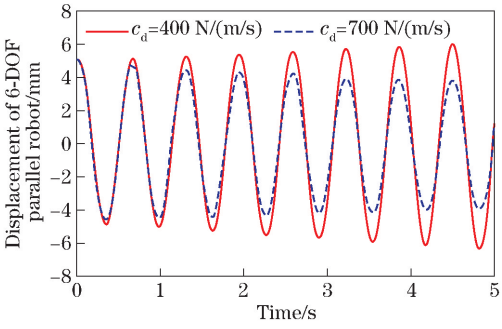

Fig. 16 Verification experiment of the stability condition

4.2.2 Comparison of simulation range of k/c

Based on the above analyses and Eq. (22) and Eq. (28), the F system and F-L system can relax the limitations of physical parameters by adjusting the parameters of the manipulator, such as mass, stiffness and damping. Therefore, they can simulate a higher range of k/c. The range of k/c that can be simulated reflects the simulation capability of the system. The conclusion with the parameters in parameter-2 of Tab. 1 is verified, and the displacement curves are shown in Fig. 17.

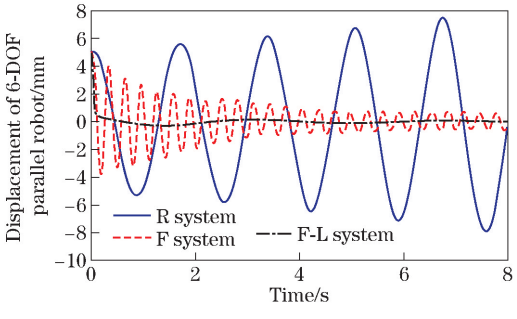

Fig. 17 Comparison of simulation range of k/c

The parameters of the three systems satisfy the condition stipulating that k/c should be greater than K_v. The curves show that the R system is unstable and the F system and F-L system are stable.

4.2.3 Influence of different forms of manipulator on improving system characteristics

Based on the above analyses, the F system adds a second order differential and oscillation elements, which provides the positive phase angle in low-frequency and mid-frequency regions synthetically. Thus, the phase margin of the F system is larger than that of the R system, such that the F system improves the stability of the system. The second order oscillation element is modified into a first order inertial element in the F-L system, which changes the amplitude and phase characteristics, making the phase margin of the system further increase. Thus, increasing the probability that a system with better characteristics will occur. Therefore, the F-L system has better stability under the same experimental parameters. In summary, the flexibility of the manipulator can improve the stability of the system. On the basis of the flexible manipulator, the HIL system, which neglects the mass of the manipulator has better stability than the other two systems.

Take the parameters in parameter-3 of Tab. 1 as an example to illustrate the validity of the conclusion. The F-L system equates m_1 to zero. The R system makes m_3 equal 10 400 kg and without stiffness and damping parameters of the manipulator. Based on frequency domain analyses, the phase margins of three models are 5°, 15° and 20°, respectively. The theoretical displacement curves (without the parallel robot participation) of the three conditions are shown in Fig. 18.

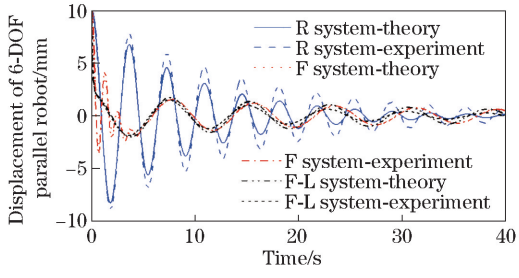

Fig. 18 Displacement results of different forms of manipulator under the same parameters

Under the same parameters, the phase margin of the R system is minimal, the dynamics displacement curve converges the slowest and the reproduction accuracy is lowest. The phase margin of the F system increases and the F system has two dynamics frequencies. Fig. 18 shows the

F system displacement curve converges quickly to the theoretical curve after the initial oscillation. Because the phase margin of the F-L system is the largest, the dynamics displacement curve can converge to the theoretical curve in the initial stage and the reproduction accuracy is high.

4.3 Comparison of dynamics frequency range based on stability and reproduction accuracy

Take the parameters in parameter-4 of Tab. 1 as an example to illustrate the validity of the conclusion in Eq. (30). The dynamics frequencies are low when the models employ the bold parameters described in parameter-4 of Tab. 1. The displacement curves are shown in Fig. 19 and the main results in Tab. 2.

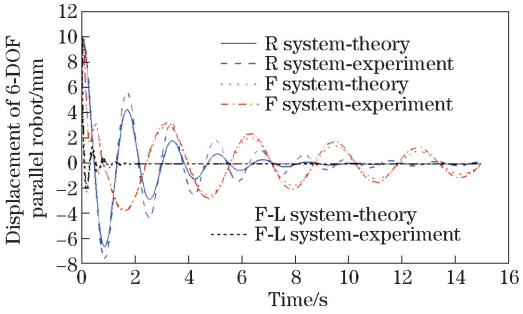

Fig. 19 Experiment results of systems in low frequencies

Tab. 2 Low-frequencies experiment results

Characteristic index	Phase margin/(°)	Dynamics frequency/Hz	Reproduction deviation/%
R system	11	0.60	14.7
F system	14	1.8(high)	10.2
F-L system	96	2.35	9.5

The frequency of the F system in Tab. 2 is the high dynamics frequency. The amplitude of the high-frequency oscillation is very small in the F system, and it decays rapidly under dampening. Thus, the F system mainly reflects the low-frequency oscillation. The relations between the dynamics frequency and the bandwidth frequency of the parallel robot are

$$\begin{cases} \text{R system: } \omega_0 = 0.06\omega_b \\ \text{F system: } \omega_{0high} = 0.18\omega_b \\ \text{F-L system: } \omega_0 = 0.235\omega_b \end{cases} \tag{31}$$

The dynamics frequency is high when the models use Tab. 1 parameters-4 noted in italic. The displacement curves are shown in Fig. 20. The main results are shown in Tab. 3.

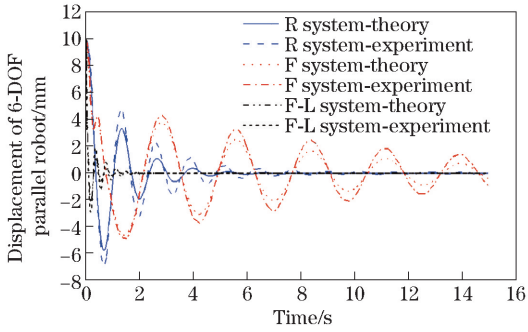

Fig. 20 Experiment results of systems in high frequencies

Tab. 3 High-frequencies experiment results

Characteristic index	Phase margin/(°)	Dynamics frequency/Hz	Reproduction deviation/%
R system	13	0.77	20.8
F system	9	2.1(high)	16.2
F-L system	32	2.57	15.2

The relations between the dynamics frequency and the bandwidth frequency of the parallel robot are as follows

$$\begin{cases} \text{R system: } \omega_0 = 0.08\omega_b \\ \text{F system: } \omega_{0high} = 0.21\omega_b \\ \text{F-L system: } \omega_0 = 0.257\omega_b \end{cases} \tag{32}$$

The results show that when the dynamics frequency exceeds the frequency range in Eq. (30), the reproduction deviation of the R system is more than 15% and the reproduction deviation of F-L system increases to 15.2%, while the phase margin is obviously reduced. When the high dynamics frequency of the F system exceeds the frequency range, the low-frequency reproduction deviation is increased to 16%. Therefore, in order to ensure better stability and reproduction accuracy, the dynamics frequencies should not exceed the results shown in Eq. (30). Based on the experimental results, the F-L system has better characteristics and reproducibility. Mass m_1 can be ignored when m_1 is far smaller than m_3 or in the case where the fundamental frequency charac-

teristic of the dynamics is the only requirement to be reproduced. Thus, the F system can be converted into the F-L system which is able to simulate more working conditions.

5 Conclusions

In this paper, the HIL simulation system model of the space manipulator docking was established. The stability of the system under different forms of the manipulator is analyzed, and the influence of different forms of manipulator on the system characteristics is analyzed and verified experimentally. The main results are as follows.

The parameter configuration relations of the F system and the F-L system are obtained as shown in Eq. (20), Eq. (25) and Eq. (26) when the HIL system has better characteristics.

The stability conditions of the R system, the F system and the F-L systems are obtained, as shown in Eq. (16), Eq. (22), Eq. (27) and Eq. (28). From these equations, the physical stiffness, damping and parallel robot open-loop speed gain should meet a certain relation to ensure the stability of the R system. Considering the flexibility, the F system could relax the restrictions on the physical parameters by adjusting the parameters of the manipulator to ensure the stability of the F system. Compared to the other two systems, the F-L system not only relaxes the physical parameters, but also has higher system accuracy and simulation ability.

The dynamics frequency simulation ability of the three HIL systems and the relationship between the dynamics frequency and the bandwidth frequency of the parallel robot are analyzed, the results of which are shown in Eq. (30). The results indicate that the F system, which considers the flexibility of the manipulator into account, can simulate higher dynamics frequencies relative to the R system on the premise of ensuring stability and accuracy. The F-L system has the best characteristics which can simulate higher physical stiffness and dynamics frequency.

This work provides a theoretical basis for the effective simulation of the HIL simulation system and a thought for transforming different forms of manipulator to obtain better system characteristics is put forth. In future works, we will mainly focus on the system delay problem to improve the instability and accuracy of the systems.

References:

[1] Zhang K F, Zhou H, Wen Q P, et al. Review of the development of robotic manipulator for international space station [J]. Chinese Journal of Space Science, 2010, 30(6): 612 – 619.

[2] Zhang W H, Ye X P, Ji X M, et al. Development summarizing of space robot technology national and outside[J]. Flight Dynamics, 2013, 31(3): 198 – 202.

[3] Feng F, Liu Y, Liu H, et al. Design schemes and comparison research of the end-effector of large space manipulator[J]. Chinese Journal of Mechanical Engineering, 2012, 25(4): 674 – 687.

[4] Pan D, Wei C, Tian H, et al. Capturing dynamics and experiment of the space large end effector[J]. Journal of Astronautics, 2014, 35(10): 1120 – 1126.

[5] Jie D, Ni F L, Tan Y, et al. Capture strategy based on a distributed control system for a large-scale space end-effector[J]. Robot, 2011, 33(4): 434 – 439. (in Chinese)

[6] Yoneyama K, Shiraki K, Ono Y, et al. Japanese experiment module (JEM) program overview[C]// Space Programs and Technologies Conference. Reston, VA, USA: AIAA, 1992: 1309.

[7] Ananthakrishnan S, Teders R, Alder K. Role of estimation in real-time contact dynamics enhancement of space station engineering facility[J]. IEEE Robotics & Automation Magazine, 1996, 3(3): 20 – 28.

[8] Ma O, Flores-Abad A, Boge T. Use of industrial robots for hardware-in-the-loop simulation of satellite rendezvous and docking [J]. Acta Astronautica, 2012, 81(1): 335 – 347.

[9] Grimbert D. Dynamic testing of a docking system [C]// Proc 1st European In-Orbit Operations Technology Symposium, 1987: 281 – 288.

[10] Elfving A, Fehse W. Simulation tools for the development of an autonomous rendezvous and docking

system[J]. ESA Journal, 1987, 11: 197 –214.

[11] Yang H, Xie Z, Sun K, et al. Development of ground experiment system for space end-effector capturing the floating target in 3-dimensional space [J]. Industrial Robot: An International Journal, 2015, 42(4): 347 –358.

[12] Yang H, Jin M, Xie Z, et al. Ground micro-gravity verification of free-floating non-cooperative satellite docking[C]//2015 IEEE International Conference on Advanced Intelligent Mechatronics. Piscataway, NJ, USA: IEEE Press, 2015: 1253 –1258.

[13] Qi C, Gao F, Zhao X, et al. Low-order model based divergence compensation for hardware-in-the-loop simulation of space discrete contact[J]. Journal of Intelligent & Robotic Systems, 2017, 86(1): 81 –93.

[14] Qi C, Gao F, Zhao X, et al. A force compensation approach toward divergence of hardware-in-the-loop contact simulation system for damped elastic contact[J]. IEEE Transactions on Industrial Electronics, 2017, 64(4): 2933 –2943.

[15] Zebenay M, Boge T, Krenn R, et al. Analytical and experimental stability investigation of a hardware-in-the-loop satellite docking simulator [J]. Proceedings of the Institution of Mechanical Engineers, Part G: Journal of Aerospace Engineering, 2015, 229(4): 666 –681.

[16] Chang T, Cong D, Ye Z, et al. Interface issues in hardware-in-the-loop simulation for spacecraft on-orbit docking[C]//IEEE International Conference on Control and Automation. Piscataway, NJ, USA: IEEE Press 2007: 2584 –2590.

[17] Zhao H, Zhang S. Stability research of space docking dynamics simulation based on Stewart platform[J]. Machine Tool & Hydraulics, 2006(8): 1 –7.

[18] Yan H, Han J, Tong Z, et al. Hybrid realtime simulation of the space docking process [C]//16th IEEE International Conference on Artificial Reality and Telexistence-Workshops. Piscataway, NJ, USA: IEEE Press, 2006: 323 –327.

[19] Huang Q T, Jiang H Z, Zhang S Y, et al. Spacecraft docking simulation using hardware-in-the-loop simulator with Stewart platform[J]. Chinese Journal of Mechanical Engineering, 2005, 18(3): 415 –418.

[20] Huang Q T, Han J W, He J F. Dynamics modeling of a six-degree- of-freedom parallel platform and its analysis. [J]. Mechanical Science and Technology, 2006(25):382 –385.

[21] Zhang S Y, Zhao H, Han J W. Direct and reverse algorithms for real-time control of 6-DOF platform [J]. Machine Tool & Hydraulics, 2003(3): 133 –135.

(**Edited by** Jianying Cai)